Thermal diffusion of lithium implanted in small and large grain boron carbide

M. Bousseksou, G. Gutierrez, Y. Pipon, D. Gosset, Nathalie Moncoffre

Thermal diffusion of lithium implanted in small and large grain boron carbide

M. Bousseksou[1,2], G. Gutierrez[1], Y. Pipon[2,*], D. Gosset[3], N. Moncoffre[2]

[1] CEA, DES/SRMP JANNUS, Université Paris-Saclay, F-91191 Gif-sur-Yvette, France.

[2] IP2I, CNRS, Université Lyon 1, F-69622, Lyon, France.

[3] CEA, DES/SRMA LA2M, Université Paris-Saclay, F-91191 Gif-sur-Yvette, France.

*: corresponding author.

Abstract

Boron carbide (B_4C) is used as a neutron absorber for nuclear reactor control and installation protection in most types of reactors. When the B_4C is irradiated in the reactor, large quantities of lithium and helium (up to about 10^{22} /cm^3) are produced due to the neutron absorption reaction ^{10}B (n, α) ^7Li. This work aims at studying the Li diffusion in large grain size (20–50 µm) or small grain size (0.2 – 5 µm) B_4C in the temperature range of 500–800 °C. Lithium was implanted in B_4C samples at a fluence of 10^{14} ions/cm^2 (maximum concentration of 54 at. ppm). The Li concentration profiles as a function of depth were obtained before and after each heat treatment by Time-Of-Flight Secondary Ionization Mass Spectrometry technique. A heterogeneous diffusion process was observed depending on the implantation depth. Considering diffusion in the non-damaged, bulk material beyond the implanted zone, the thermal diffusion of lithium into the grain boundaries was found to be about four orders of magnitude higher than into the grains.

Keywords: boron carbide, diffusion, lithium, TOF-SIMS.

Highlights

- TOF-SIMS analyses of Li have been performed in implanted and annealed high density, large grain boron carbide.
- The diffusion coefficient of Li in boron carbide has been determined in the 500 – 800°C range, the obtained activation energy, about 2 eV, is close to ab initio estimations.
- Li diffusion is highly enhanced in the gain boundaries.

1 Introduction

Boron carbide (B_4C) is a very hard refractory ceramic (hardness of about 30 GPa) [1, 2] with a high melting temperature around 2400 °C [3]. Its crystal structure was first characterized in 1943 by Clark *et al*. [4] following X-ray diffraction experiments [5]. It consists of nearly regular icosahedra of 12 atoms (composition mainly $B_{11}C$) which are connected in a rhombohedral network with a space group $R\bar{3}m$. Connected to the icosahedra, a linear chain (composition mainly C–B–C) is located on the main diagonal of the rhombohedra leading to $B_{12}C_3$ cells (hence the B_4C formula). B_4C is employed as a neutron absorber in most types of nuclear reactors [6] and specifically in fast neutrons ones. Its use as a neutron absorber is permitted by the high neutron absorption cross section of the boron-10 isotope ^{10}B (a few barns for fast neutrons [7]) with a natural concentration of about 19.8 at. %, possibly enriched depending on the applications. Under neutron irradiation, the (n, α) absorption reactions on the boron-10 isotope result in the production of large quantities of light elements such as helium and lithium (up to about 10^{22} /cm^3 [8]). Most studies [9, 10, 11, 12] have focused on the behavior of helium in boron carbide, which is now well understood. Helium is accumulated in the form of highly pressurized bubbles, both in the grains and at the grain boundaries of the material, which induce swelling and micro-cracking. Motte *et al.* [13] have observed that helium clusters form either on structural defects (efficient grain boundary trapping) or thanks to irradiation damage induced nucleation. Therefore, the damage favours the germination of clusters of helium. However, the behavior of lithium and the associated diffusion mechanisms are still to be studied as only a few papers have addressed this topic.

Kervalishvili *et al.* [14] studied the diffusion of lithium in porous boron carbide samples (~93% density) obtained by hot pressing. Lithium was then introduced into the material by impregnation before being annealed at different temperatures. The authors deduced two lithium diffusion mechanisms that were attributed to volume diffusion and grain boundary diffusion, with activation energies of 0.37 eV and 0.13 eV, respectively. A second study was carried out by Deschanels *et al.* [15]. A high density (~96%) boron carbide material with grain sizes inferior to 10 µm was irradiated at low fluence (^{10}B burnup = 2.5×10^{21} captures/cm^3) at temperatures ranging from 500 to 700 °C in the French *Phénix* fast neutron reactor. The nuclear microprobe was used to analyse the Li depth profiles in post-irradiation annealed discs. The authors identify two diffusion mechanisms with activation energies of 0.88 eV (related to intragranular diffusion) and 0.19 eV (related to fast diffusion through grain boundaries and micro-cracking). The lithium retention in neutron irradiated B_4C as a function of ^{10}B burnup was analysed by Brocklehurst *et al.* [16] on B_4C pellets (theoretical densities ~98%) of the MK-II control rods of the British PFR (Prototype Fast Reactor) reactor at a temperature about of 600 °C. They showed that the lithium retention is close to 100% for a neutron capture density of 2.5×10^{21} captures/cm^3, then it

decreases to about 90% for a neutron capture density of 4×10^{21} captures/cm^3. Hollenberg [10] analysed boron carbide samples irradiated in the EBR-II reactor in a temperature range between 565 and 985 °C with a capture density of 70×10^{20} captures/cm^3. The lithium retention was 87% for pellets enriched to 92% ^{10}B and 92% of the theoretical density. Oakden *et al.* [17] studied also the lithium retention in B_4C samples (theoretical densities ~88%) as a function of burnup. These pellets were irradiated at elevated temperatures (> 600 °C) in the UK PFR reactor for a capture density ranging from 2.75×10^{21} at/cm^3 to 7.5×10^{21} at/cm^3. They observed that, from the beginning of irradiation, the retention rate of lithium is very high (quasi-total).

This review of the available literature shows the lack of experimental results obtained in parameterized and controlled conditions to understand fundamental aspects of the lithium diffusion behavior in boron carbide. Atomistic modelling techniques can bring valuable data to explore diffusion mechanisms. To our knowledge, there are no B-C empirical potentials, which means that molecular dynamics cannot be performed in time and temperature ranges allowing to identify diffusion pathways and associated diffusion coefficients. An alternative consists in performing ab initio calculations with pre-built diffusion pathways. Thanks to different methods (nudged elastic band, linear synchronous transit/quadratic synchronous transit…), an activation energy associated to the pre-built diffusion pathways can be calculated. If point defects and helium migration in B_4C have been widely studied by ab initio calculations (see for instance Schneider *et al*. [18]), only one study can be found for the lithium migration. You *et al.* [19] have investigated migration energies for the lithium interstitial-type defects. Based on the classical $B_{11}C$-CBC boron carbide cell model, they have calculated a barrier of ∼1 eV for the lithium atoms migrating among the interstitial sites in the $(111)_{rh}$ planes of the rhombohedral structure (then leading to a two-dimension diffusion regime) and a barrier of ~2-2.5 eV for the lithium atoms migrating out the (111) planes, then allowing a three-dimension diffusion regime.

In that context, we have realised a fundamental parametric study to determine lithium thermal diffusion mechanisms in the volume of B_4C and sought to determine if grain boundaries in the material could modify the long-range diffusion. To limit the role of damage, lithium was implanted at low concentration (below 54 at. ppm) in dense boron carbide pellets. Time-of-flight secondary ion mass spectrometry (TOF-SIMS) was then used to determine the Li concentration versus depth. From the evolution of those profiles, diffusion coefficients for temperatures ranging from 500 to 800 °C were determined. It should be noted that the temperature range was chosen to be close to the one in the absorber pellets during SFR (Sodium-cooled Fast-neutron Reactor) operating conditions. At last, an Arrhenius law was used to deduce the corresponding activation energy; this is then compared with literature data.

2 Experimental procedure

High density B_4C pellets (over 98% of the theoretical density) were prepared at the Extreme Materials Technologies Laboratory (LTMEx) at CEA Saclay by SPS (Spark Plasma Sintering). The BAM ERM powder was used. This is a reference powder [20] with good purity (99.7 %), slight under-stoichiometric ($B_{3.8}C$) and with large grain sizes (10–50 µm). To study lithium diffusion into the grain boundaries, the Starck HD20 powder was used. In this case, a high density of grain boundaries into the implanted zone and its vicinity was desired. The grain size of this powder is lower than 0.5 µm, the stoichiometry and impurities content are different from the ERM powder (Table 1).

Table 1. Selected properties of the materials

Material	ERM	HD20
Supplier	BAM	H.C. Starck
SPS sintering: T (°C)	2200	1850
p (MPa)	40	75
t (min)	2	5
Density (%)	97	95
Pellet grain size (µm)	10 - 50	0.2 - 5
Composition: B (w.%)	78.5	76.0
C (w.%)	21.0	22.2
O (w.%)	0.1	1.3

For the ERM powder, sintering was performed at 2200 °C in vacuum for 2 min at a 40 MPa pressure in a graphite die. For the HD20 powder, the conditions are slightly different, in order to limit the grain growth. After sintering, cylindrical B_4C pellets of 20 mm diameter and 5 mm height were obtained. Using a diamond wire saw, the pellets were cut into discs with a thickness of 800 µm. The discs were further polished with diamond pastes until a mirror surface is obtained. Then, the boron carbide discs were annealed at 800 °C for 5 h in vacuum in order to anneal and reduce the density of the polishing-induced defects.

Lithium ions were then implanted at room temperature at the SCALP Orsay facility of IJCLab [21], using the IRMA ion implanter at a 170 keV energy ~~for~~ and a fluence of 1×10^{14} at/cm^2. The Li distribution and the displacements per atom (dpa) as a function of depth (Figure 1) were calculated by the SRIM (Stopping and Range of Ions in Matter) [22] software in the « full cascade mode ». We considered a B_4C density of 2.52 g/cm^3 and the threshold energies of displacement of boron and carbon atoms were

taken from Zuppiroli *et al.* [23]; that is 20 eV for B and C. The resulting Li profiles are quasi-Gaussian with a projected range (Rp) of 620 nm. At a fluence of 1×10^{14} at/cm^2, the maximum concentration is 0.0054 at.%. The maximum damage is located at a depth of around 600 nm for a value of 0.0057 dpa.

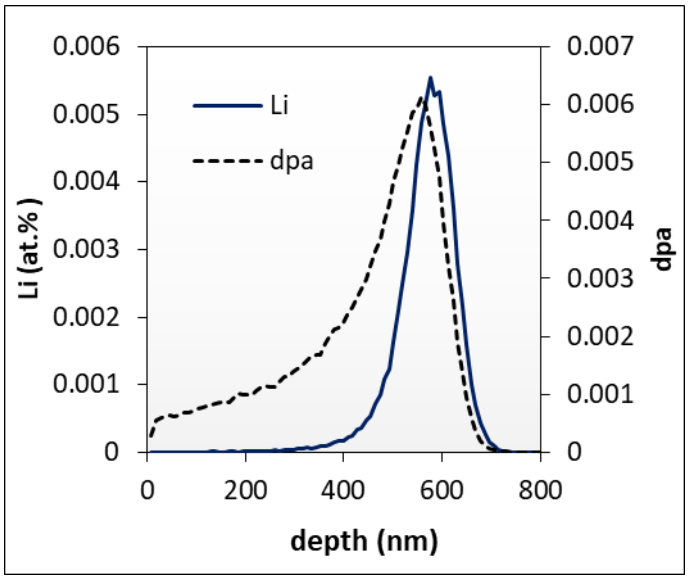

Figure 1: SRIM calculations of the Li concentration (at.%) and irradiation damage (dpa) profiles with respect to depth for a Li implantation energy of 170 keV and a fluence of 1×10^{14} at/cm² (depth corrected from SIMS results).

In order to analyse the role of the grain boundaries in HD20 materials, the grain size distribution has been measured and is reported in Figure 2 along with a fit by a log normal curve. Assuming that grain size of the ERM samples (at least 10 µm) was larger than the Li depth profile, no grain size distribution was determined for these samples.

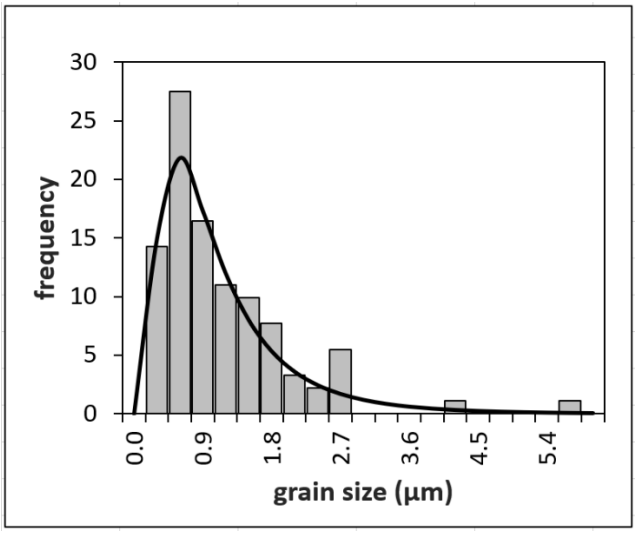

Figure 2: Grain size spectrum of the HD20 discs fitted with a log-normal distribution.

After implantation, heat treatments were performed in the 500–800 °C temperature range (accuracy of ± 10 °C) and under secondary vacuum at a pressure of 10^{-7} mbar. In order to obtain the Li concentration profiles as a function of depth, the samples were analysed by TOF-SIMS before and after each heat treatment at "Science et surface, SERMA Technologies'' in Lyon. The instrument is a TOF.SIMS 5 from IONTOF. Two pulsed primary ion beams were alternately used to perform dynamic SIMS measurements. An oxygen ion beam (O^{2+}) of 1 keV, with a current set to ~500 nA, scanning an area of about 150×150 µm^2 is sent to the sample surface to sputter a crater of a few nanometers in depth at each cycle. For the analysis, a short pulse of a 25 keV bismuth (Bi^+) ion beam with a current of 1.5 pA is sent at each sputtering step in the centre of the crater over an area of 50×50 µm², in order to avoid any wall effect of the crater: this means only a few B_4C grains are analysed on a given crater, making the possible influence of the grain boundaries quite low. The Bi-sputtered ions are then analysed in a mass spectrometer. The main analysed species in our study are: $^7Li^+$, $^{10}B^+$ and $^{12}C^+$ (Figure 3).

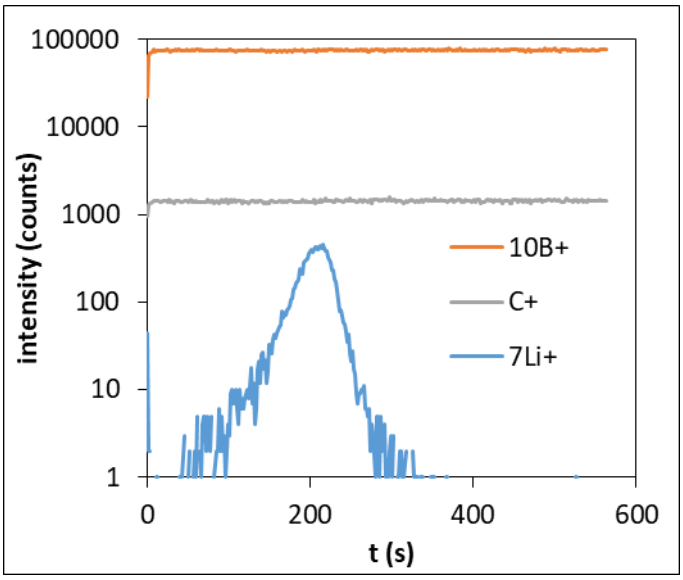

Figure 3: Chronograms of $^7Li^+$, $^{10}B^+$ and $^{12}C^+$ species in a 1×10^{14} at/cm^2 Li implanted B_4C sample.

The obtained chronograms represent the signal intensity of each element detected as a function of time. In order to obtain concentration profiles (at. %) as a function of depth (nm), a two-step approach is used:

The crater depth was determined by optical interferometry at the LaMCoS laboratory of INSA Lyon. The instrument used is a profilometer of Sensofar Neox. By knowing the depth, we can calculate a mean sputtering rate (Eq. (1)).

$$Sputtering\ velocity = \frac{crater\ depth}{final\ acquisition\ time} \qquad Eq.\ (1)$$

Assuming a constant sputtering ~~velocity~~ rate then allows the time to depth conversion.

The atomic lithium concentration was obtained using the RSF (Relative Sensitivity Factor) method developed by Wilson [24] (Eq. (2)).

$$RSF = \frac{\varphi \times \overline{I_B}}{\left(\sum_{i=0}^{final\ time} I_i - I_{bgd} \times n_{cycle}\right) \times t_{cycle} \times V_{sputter}} \qquad Eq.\ (2)$$

With:

φ: implantation fluence in at/cm^2.

$\overline{I_B}$: averaged $^{10}B^+$ signal taken as an internal reference in counts.

$\sum_{i=0}^{final\ time} I_i$: sum of the secondary ion counts of the implanted isotope ($^7Li^+$) over the depth profile.

I_{bgd}: background ion intensity of I_i in counts/data cycle.

n_{cycle}: number of data cycles over the depth profile.

t_{cycle}: analysis time in s for one cycle.

$v_{sputter}$: sputtering rate in cm/s.

This then allows converting the Li signal to Li relative concentration to the reference element, here ^{10}B. For each TOF-SIMS analysis of a given sample, two or three craters were made in order to ensure a good reproducibility of the signal.

3 Results

3.1 Large grain material (ERM)

The evolution of the lithium depth profiles obtained by TOF-SIMS in B_4C samples implanted at a fluence of 1×10^{14} at/cm^2 after annealing from 500 to 800 °C between 30 min to 4 h are compared to the as-implanted profile in Figure 4. From the comparison of the areas of the as-implanted profile with the annealed ones, a global loss of lithium has been calculated at each annealing temperature: 0% at 500°C, 10% at 600°C, 20% at 700°C and 50% at 800°C. The error associated for each loss is ±10%.

The thermal treatment at 500 °C induces a small broadening only on the right (deep) part of the Li profile (Figure 4.a). Then, at 600 and 700 °C, the following significant modifications are observed: a strong broadening and a sharp decrease of the Li concentration at around 500 nm (Figure 4.a). The profile after annealing at 800 °C for 1 h 40 (Figure 4.b) shows the same characteristic shape with a very

important widening towards the depth of the material reflecting a fast diffusion and a sharp decrease of Li concentration. The Li loss becomes significant (at least equal to the associated error) at 600°C from the moment the Li depth profile is broad enough to reach the surface. This indicates that only a very small fraction of Li can escape through the porosities or the grain boundaries in the ERM samples.

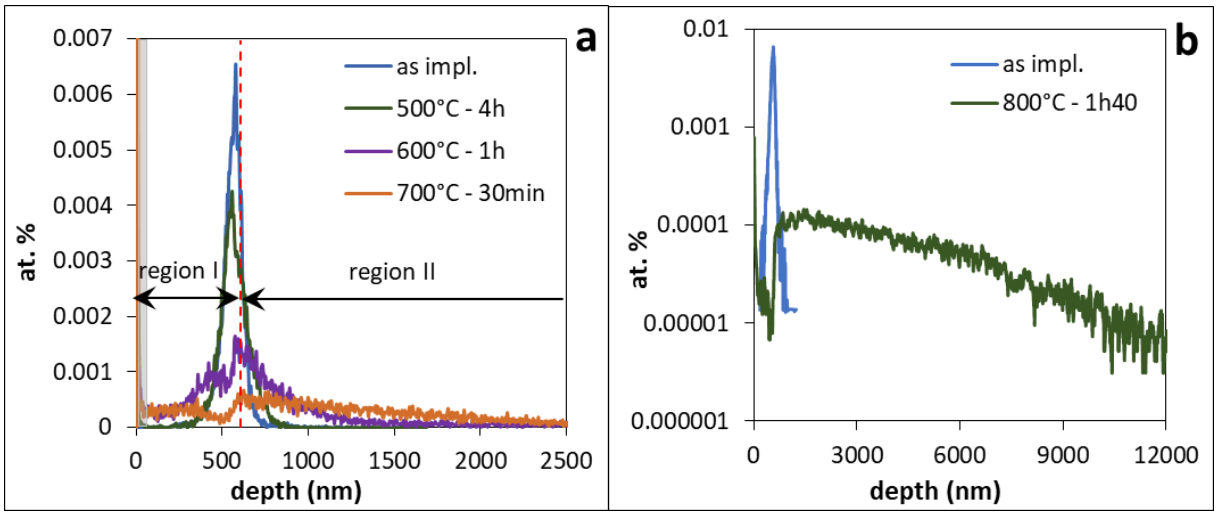

Figure 4: Lithium distribution profiles in B_4C implanted with 170 keV Li^+ ions at 1×10^{14} at/cm^2 and annealed (a) from 500 to 700 °C between 30 min to 4 h and (b) at 800°C for 1 h 40 (log scale). The grey band in Figure 4.a corresponds to the first points up to~50 nm, for which surface effects make the profile unusable. The dashed red line delimits the two regions of interest (I and II).

A heterogeneous evolution as a function of depth is observed on all profiles and two different regions are identified as shown in Figure 4.a:

- A first region from the surface at low depth (named region (I)), where the profile shape is rather complex. A second region on the right side of the profiles (named region (II)). This region is located beyond the implantation peak.

In a first approach, we only considered region (II). A simple, thermally activated diffusion of Li was assumed. As mentioned above, the Li implanted profile has a quasi-Gaussian shape. Consequences of the Fick's laws for such Gaussian profiles then allowed us fitting each depth profile in this region using half-Gaussian curves. An example of such Gaussian adjustments is illustrated in Figure 5 for the profile determined after annealing at 700 °C during 30 min.

In that case, an apparent diffusion coefficient was determined (Eq. (3)) using the Fick's second law for a Gaussian distribution:

$$D(T) = \frac{\sigma_f^2 - \sigma_i^2}{2\Delta t} \qquad \textit{Eq. (3)}$$

With:

D (T): apparent diffusion coefficient at a temperature T.

σ_f: standard deviation of the gaussian after annealing at temperature T and duration Δt.

σ_i: standard deviation of the gaussian before annealing.

Thus, from the widening between the as-implanted profile and the profiles after annealing, we can deduce an apparent diffusion coefficient for each temperature using equation (3). The obtained results are reported in Table 2.

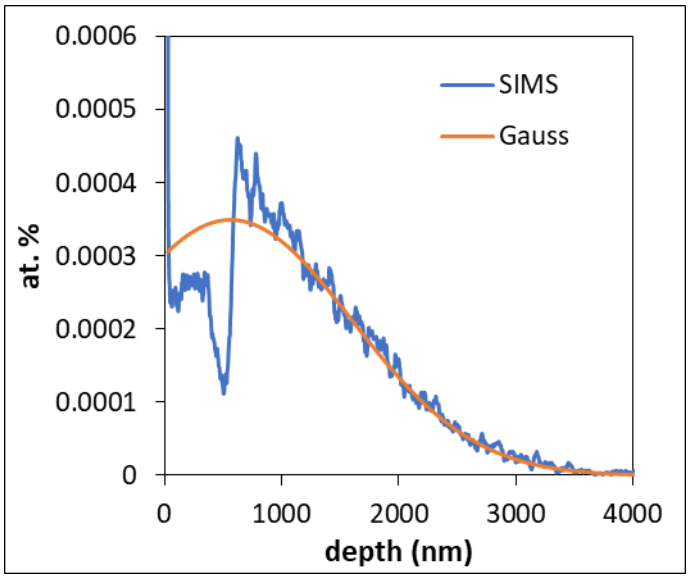

Figure 5: Example of SIMS profile fitting (half-gaussian in region II) of the Li implanted B_4C sample (10^{14} at/cm^2) and annealed at 700 °C for 30 min.

Table 2: Li apparent diffusion coefficients in B_4C (m²/s) as a function of annealing conditions.

Annealing conditions	Li apparent diffusion coefficients (m²/s)
500 °C – 4h	$(2.4 \pm 0.2) \times 10^{-19}$
600 °C – 1h	$(1.5 \pm 0.3) \times 10^{-17}$
700 °C – 30min	$(2.7 \pm 0.2) \times 10^{-16}$
800 °C – 1h40	$(2.0 \pm 0.2) \times 10^{-15}$

The uncertainties on the diffusion coefficients u(D) have been calculated thanks to the following equation:

$$u^2(D) = \left(\frac{\partial D}{\partial \sigma_f}\right)^2 . u^2(\sigma_f) + \left(\frac{\partial D}{\partial \sigma_i}\right)^2 . u^2(\sigma_i) + \left(\frac{\partial D}{\partial \Delta t}\right)^2 . u^2(\Delta t) \qquad \textit{Eq. (4)}$$

We can assume the main error comes from the fit of the Gaussian part of the profiles after annealing. Therefore, the diffusion coefficient uncertainties have been calculated thanks to the following equation:

$$u^2(D) \sim \left(\frac{\sigma_f}{\Delta t}\right)^2 . u^2(\sigma_f) \qquad \textit{Eq. (5)}$$

With $u(\sigma_f)$ being determined by the error associated to the automatic fit (Origin software).

For a given diffusion mechanism, the evolution of the apparent diffusion coefficient as a function of temperature is defined by the Arrhenius equation (Eq. (6)).

$$D(T) = D_0 . exp\left(\frac{-E_a}{k.T}\right) \qquad \textit{Eq. (6)}$$

With D_0 the pre-exponential factor, E_a the activation energy (in eV) and k the Boltzmann constant (8.617×10^{-5} eV/K).

As shown in Figure 6, the D(T) points for each Li fluence are aligned, meaning only one diffusion mechanism is activated. Eq. 6 can then be used to estimate the activation energy (E_a) of 2.16 ± 0.08 eV (error is deduced only from the fit).

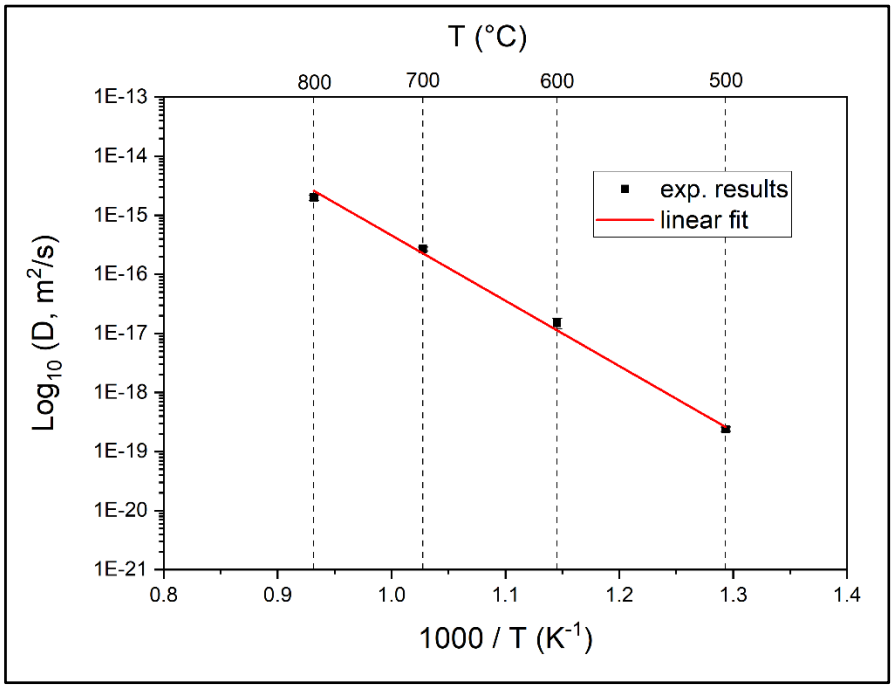

Figure 6: Arrhenius diagram of the apparent diffusion coefficient of Li in B_4C (except for the 600°C value, error bars are smaller than the symbol size).

3.2 Small grain material (HD20)

In order to assess the impact of the grain boundaries on the thermal diffusion of Li in B_4C, HD20 samples have been implanted with 170 keV Li and subsequently annealed for 30 min at 700°C. Typical lithium SIMS profiles are reported in Figure 7. Only one reference profile has been reported as the HD20 and ERM as-implanted profiles are identical.

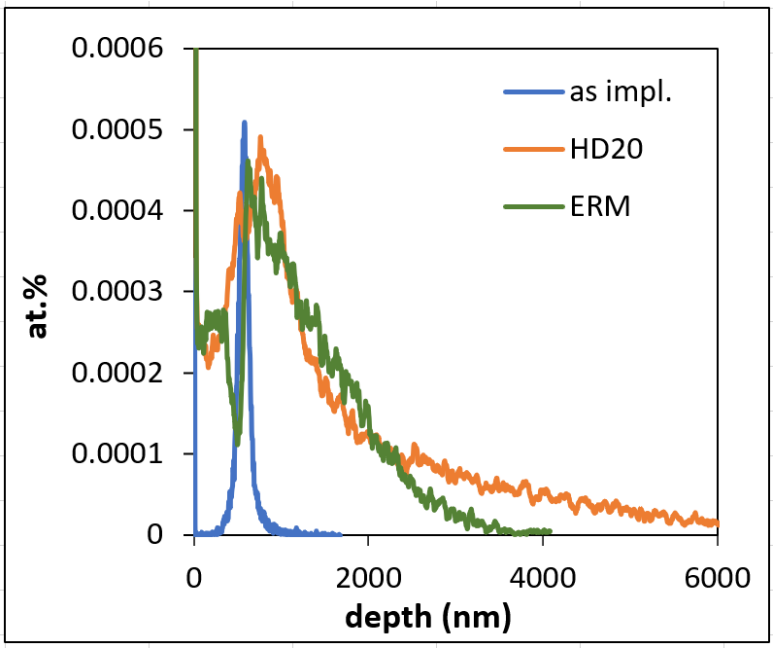

Figure 7: SIMS profiles of Li implanted in B_4C, before and after annealing at 700°C. Comparison of Li profiles after annealing in HD20 and ERM materials (see also Figure 4) and before annealing (as implanted signal).

It clearly appears that after annealing, the HD20 and ERM profiles are different. In both materials, the maxima of the Li profiles are shifted towards the depth compared to the as-implanted profile: this could be related to desorption effects leading to a wide depleted zone. In the HD20, the profile shows a slope change around 1500 nm and the trough located around 500 nm observed on the ERM profile has nearly disappeared. At first glance, the profiles beyond the implantation peaks have a gaussian shape, but with different tails. The different widths indicate that the diffusion coefficient in the HD20 material is lower than in the ERM. This could arise from slightly different compositions (e.g., oxygen content). On the other hand, considering the grain size distribution of the HD20 material, it is clear that the lithium profile is wider than the distribution of grains around the implanted zone. It can then be deduced that Li is not significantly trapped by the grain boundaries, unlike helium [13]. Assuming a normal diffusion, the Fick laws apply and the profile can be fitted with a gaussian. From its width, a diffusion coefficient of about 3.2 10^{-13} cm^2/s is deduced.

To explain the long tail of the HD20 Li profile, we assume an accelerated grain boundary diffusion, with possible Li exchanges between the grains and the grain boundaries. Le Claire [25, 26, 27] has developed a formalism able to take such processes into account, this allowing an estimation of the diffusion coefficient into the grain boundaries. In a polycrystalline material, three cases can be considered. In case A, the grain boundary diffusion is similar to diffusion in the bulk material. In case B, the grain boundary diffusion is significantly higher than in the bulk material. In case C, the grain boundary diffusion is so high that the bulk diffusion can be neglected. Let us determine to which case our results can be attributed. This is not 'A' since the profile is much broader than in ERM even though the bulk diffusion coefficient is lower. To check if it is 'B', a criterion has been defined by Le Claire:

$$s\,\delta \ll \sqrt{D_v\,t} \ll d \qquad \textit{Eq. (7)}$$

Which means the diffusion length is intermediate between an apparent grain boundary thickness and the grain size, with:

s: segregation factor, around 1 for self-diffusion and up to 10 – 50 for heterogeneous diffusion,

δ: apparent thickness of the grain boundaries, classically about 1 nm.

D_v: bulk diffusion coefficient, here 3.2 10^{-13} cm²/s for the 700°C annealing.

t: annealing duration (1800 s for the 700°C annealing)

d: grain size, here the mean of the log-normal distribution, *i.e.* 1.2 µm.

We then deduce (all dimensions in cm):

$$10^{-7} < 2.4\ 10^{-5} < 1.2\ 10^{-4}$$

which clearly satisfies the 'B' criterion.

In this case, the grain boundary diffusion coefficient can be estimated by an empirical formula:

$$s\,\delta\,D_{gb} = 1.308\sqrt{\frac{D_v}{t}}\left(-\frac{\partial\, ln\,(C)}{\partial\, x^{5/6}}\right)^{-\frac{5}{3}} \qquad \textit{Eq. (8)}$$

With:

x: depth

D_{gb}: diffusion coefficient into grain boundaries,

C: Li concentration profile,

$\partial()/\partial()$: slope of the deep Li distribution in the ln(C) versus $x^{5/6}$ frame [25].

We obtain a slope equal to – 23994 (Figure 8), from which we deduce (with s = 1) at 700°C:

$$D_{gb} = 8.7\ 10^{-12}\ m^2/s$$

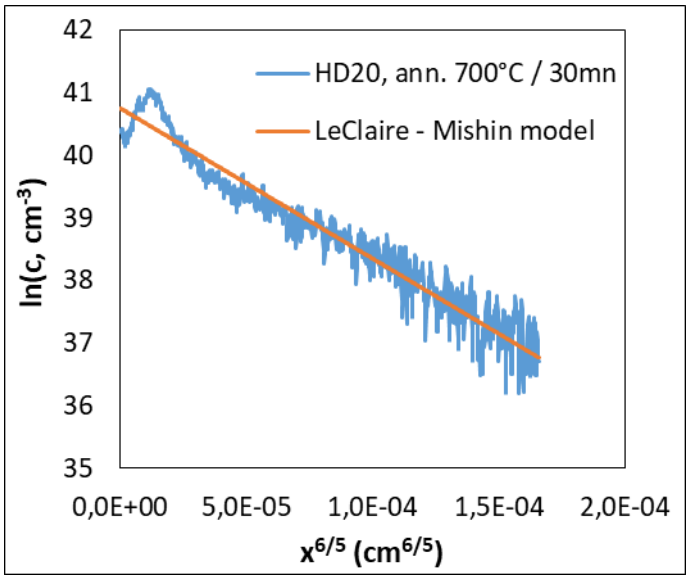

Figure 8: Li profile concentration after the annealing of the HD20 material for 30 min at 700°C in the ln(C) versus $x^{5/6}$ frame.

4 Discussion

4.1 Li diffusion comparison in HD20 and ERM samples

For all implanted and annealed samples, the Li profiles show an asymmetric broadening from both sides of the implantation peaks with a through appearing around 500 nm. The present paper focuses on the right side of the profiles which corresponds to the region II in Figure 4. This part of the sample should be free from implantation induced-defects, at least considering the SRIM data (Figure 1 shows no damage beyond a depth of 750 nm). This means that Li diffusion in region II involves either structural defects (such as Li-vacancies complexes) or simple interstitial diffusion mechanisms. Considering ERM samples, the TOF-SIMS profiles are obtained on surfaces including only a few B_4C grains and the crater depths are much smaller than the grain size. This means that possible diffusion at grain boundaries - or trapping - would have a fairly small contribution here. Therefore, in a first approach, these samples are ideal to measure intragranular (or volume) diffusion. If we consider the HD20 samples, the as-implanted Li profile intercepts several different grains. This means that intra- and inter- granular diffusion could both occur in these samples. The intragranular diffusion coefficient has been calculated with the same procedure for the ERM (2.7×10^{-12} cm²/s) and the HD20 samples

(3.2×10^{-13} cm²/s). The difference is roughly an order of magnitude which can be surprising as one would have expected close values.

A similar approach to our work was carried out by Linnarsson *et al.* in silicon carbide (SiC) samples implanted at room temperature with Li at an energy of 30 keV and a fluence of 1×10^{15} at/cm^2 [28]. These samples were annealed in vacuum (~10^{-7} Torr) at a temperature of 600 °C and for durations ranging from 0.5 to 16h. SIMS was used to measure the depth distribution of Li after the heat treatment: the approach is therefore very close to ours, which enhances the interest of this study. The Li profiles are quite similar to ours: a mobile fraction of Li diffuses according to a Gaussian shape (linear plots of the logarithm of the distribution of mobile Li versus the square of the depth) and another non-mobile Li fraction remains trapped in the implanted zone. It is shown that the amount of mobile lithium as a function of annealing duration remains constant, the atoms have only rearranged and moved deeper into the sample as a function of time. Therefore, by plotting the logarithm of the distribution of mobile Li versus the square of the depth, an effective diffusion coefficient of 1.6×10^{-13} cm^2/s can be estimated at the temperature of 600 °C. This value is pretty close to ours in ERM B_4C samples at 600°C (1.5×10^{-13} cm^2/s). The authors reveal that the diffusion into the bulk is associated with the formation and dissociation mechanisms of lithium–defect complexes (lithium trapping/de-trapping mechanism in the defects). Following the same reasoning, it can be assumed that trapping/de-trapping mechanisms can lower the Li diffusion coefficient in the HD20 samples. Indeed, these samples have a higher content of grain boundaries inducing an increased concentration of vacancies in the grains. This point cannot be taken into account by SRIM calculations as the code considers only an amorphous monocrystalline layer. Another point to consider is that lithium could also be affected by the oxygen content which is ten times larger in HD20 samples and could also lower the Li diffusion.

This impact of the grain boundaries on Li diffusion in boron carbide is highlighted by the comparison of the Li depth profiles at 700°C for ERM and HD20 samples (see Figure 7). However, extracting an intergranular diffusion coefficient (i.e in the grain boundaries) is a difficult task. Mishin *et al.* [27] reconsidered Le Claire's approach. Different criteria are defined, with slightly different exponents and pre-factors, leading to slightly different results, whose differences are not significant. We will therefore consider the previous result. Our case is close to the diffusion from a surface deposit, for which Le Claire formalism has been developed: the implanted Li is close to the surface, compared to the extent of the diffused profile. The apparent grain boundary diffusion coefficient appears more than 4 orders of magnitude higher than the bulk diffusion coefficient. Higher differences can still be observed in metals [26]. Such high values are permitted by the high crystalline disorder into the grain boundaries. Moreover, due to the low stoichiometry of the HD20 material, nanometer thick graphite precipitates,

too thin to be detected by X-ray diffraction, could also be present. In that case, quite high diffusion coefficients are expected [29].

One last point to consider which can mitigate the diffusion coefficient values is an effect from the grain orientation, with either an accelerated or a slowed down diffusion depending on the grain orientation, as suggested by ab-initio calculations from You *et al.* [18]. This effect however is not observed here for the ERM samples, since the different profiles obtained on a given sample are quite similar (similar broadenings, no tails nor shoulders on the deep part of the profiles). This indicates that intragranular diffusion should not really be impacted by the grain orientation. However, this effect cannot be excluded for the intergranular diffusion. As SIMS analyses are performed on, at least 500 grains, for the HD20 samples, the deduced profile is an average of several different grain boundaries created by grains with different orientation.

4.2 Mechanisms of Li diffusion in boron carbide samples

The corresponding activation energy of ~2 eV in the temperature range of 500–800 °C is quite high compared to the experimental literature values, inferior to 1 eV [14, 15]. This difference is highlighted in the Arrhenius diagram in Figure 9.

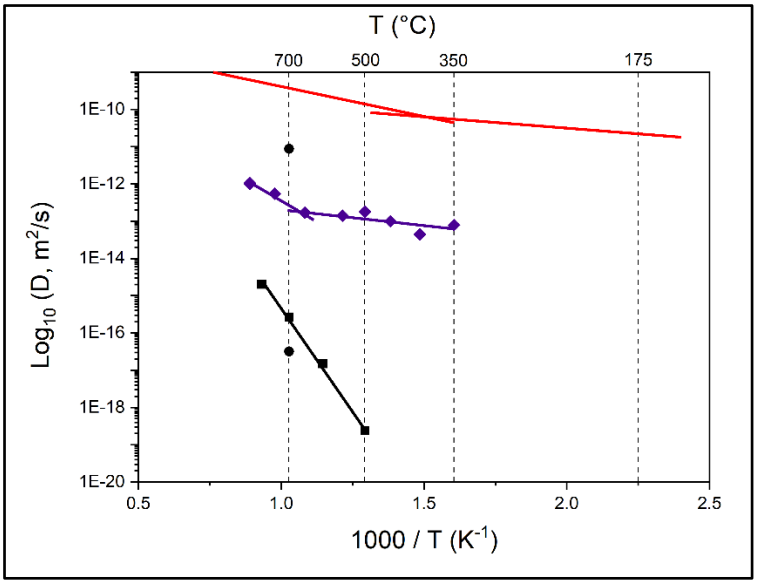

Figure 9: Lithium diffusion coefficients in boron carbide. Top curve: Kervalishvili et al. [14], in porous B_4C after surface impregnation. Mid-curve: Deschanels et al. [15], in an industrial small grain, 95% density B_4C irradiated in fast neutron reactor. Bottom curve: our results, in a large grain, 98% density B_4C after ion implantations. Black circles: our results, in HD20 samples (small grains).

Two main observations can be drawn from Figure 9. First, the intragranular diffusion coefficients in our study are much lower than those determined by Kervalishvili *et al.* and Deschanels *et al*. The experimental data available in the paper of Kervalishvili *et al.* do not indicate any grain size nor Li concentration. However, the authors indicate the presence of structural flaws and impurities in their specimens, which promotes the penetration of lithium and/or segregations along the boundaries of these defects. The samples have also a rather low density which indicates the presence of partially open porosities, which could also promote Li diffusion. These two points can explain the high diffusion coefficient values. Deschanels *et al.* have used cylindrical specimens of dense B_4C. These samples were irradiated into the Phénix fast neutron reactor. Thus, the lithium is made to diffuse in a damaged, cracked material probably with the presence of impurities (He bubbles in particular) which can explain the pretty high diffusion coefficient values. However, extrapolating their estimations to the actual life duration of B_4C control rods lead to diffusion lengths inconsistent with the retention rates observed by Brocklehurst *et al.* [16] or Oakden *et al.* [17]. Analysing large grain materials, we here observed diffusion in a non-damaged, quasi-monocrystalline material. The comparison of our experiment with those of the literature shows the importance of the presence of defects in the Li diffusion process. However, a change in the number of defects, for a same diffusion mechanism, should only impact the D_0 term as the atomic jump frequency is expected to increase with the increase of defect populations (which is the case for the Li intergranular diffusion coefficient determined in our study). This seems to indicate that the defects involved in the different studies are not of the same nature or that the diffusing species is not atomic Li.

The second information from Figure 9 comes from the different slopes in the Arrhenius plot, indicating a change in the Li diffusion mechanisms. Kervashvili *et al.* identified two regimes of diffusion: above 550 °C (volume diffusion), below 350 °C (boundary diffusion), and a mixed regime between 350 °C and 550 °C. Deschanels *et al.* identified two regimes separated at ~675 °C. It can be noted that considering the high dispersion of Deschanels *et al.* results, using only one straight line leads to the same statistical confidence; the two-regimes hypothesis could then be questioned. From our experiments, no change in the diffusion mechanism was observed from 800 °C down to 500 °C. We assume that these differences are due not only to the more or less damaged materials, but also to different diffusion mechanisms that could prevail and be activated at various temperature thresholds. Clearly, in the materials used by Kervashvili *et al.* and Deschanels *et al.*, the diffusion pathways are comparable (similar energies), even if the Li close environments are different (different D_0), and different of those which are activated in our experiments. On the other hand, Desgranges *et al.* [30] **Erreur ! Source du renvoi introuvable.**have irradiated boron carbide pellets with thermal neutrons in neutral atmosphere in the French ILL reactor. They observed micron-sized droplets at the surface, interpreted as lithium

exudation from the material, which could correspond to lithium having diffused through the grain boundaries to the surface. At last, our value of intergranular diffusion coefficient becomes comparable to that of Deschanels *et al.* [15].

In order to go further in the discussion of the mechanisms controlling the Li diffusion, a comparison with ab-initio calculations is required. You's ab-initio calculations of diffusion paths of Li in B_4C lead to two quite different diffusion energies, respectively about 1 eV along the (111) rhombohedral planes and about 2.2 to 2.4 eV along other directions [18]. We deduced an energy of about 2 eV with a rather narrow uncertainty. Indeed, even if all Li profiles are obtained from tens of grains presenting different orientations (microstructural examinations show the material is close to isotropic), we observe quite similar profiles and broadenings at a given annealing temperature. Following the results from You *et al.*, this means that, even if (He or Li) 2D diffusion occurs, the 3D diffusion mechanisms through interstitial sites around different CBC chains should be the rate-controlling mechanism. It has to be noted that a similar trend was also observed by Motte *at al.* for helium diffusion in boron carbide [31].

Finally, Li diffusion in actual materials, either with small grains and / or with irradiation-induced cracking, would be then much higher than in the bulk material. However, this raises an important issue: post-irradiation examinations of boron carbide pellets, irradiated in fast-neutron sodium cooled reactors, show a very high lithium retention [32, 16]. Different mechanisms are then to be assumed. Li could be trapped on irradiation defects, or into the helium bubbles. It could also be prevented from desorbing the material, since lithium is nearly insoluble in sodium. It would be necessary to reconsider the available results taking into account this new estimation.

5 Conclusion

This study contributes to a better understanding of lithium behavior in boron carbide, in particular the Li thermal diffusion. B_4C samples with two different grain sizes were implanted with Li ions at 10^{14} ions/cm^2. After heat treatments, the Li profiles were obtained by TOF-SIMS analyses.

The results have evidenced a broadening of the Li distributions, highlighting a classical diffusion of lithium in the deep, non-damaged zone of the material. Analysis of this part of the profiles with classical Fick's equations allows the evaluation of apparent diffusion coefficients in a temperature range from 500 to 800 °C. An activation energy of about 2 eV was deduced. In the front zone, profiles with a more complex shape have been highlighted, not yet understood. From studies performed in similar systems, we may infer the existence of damage–Li coupling and trapping/de-trapping mechanisms. By

performing the same analysis in a small grain size material, we have shown that lithium diffusion in the grain boundaries is strongly enhanced.

Complementary analyses by Raman spectroscopy to evaluate the disorder of the material as well as Transmission Electron Microscopy observations to control the microstructure of the material need to be carried out. Further studies are in progress aiming at understanding the role of defects during Li diffusion in B_4C. For that, irradiations with heavy ions such as Au ions will be used to simulate the effect of ballistic damage induced by fast neutrons in reactor. Li implantations at higher fluences will also be performed in order to study possible Li-Li interactions.

Acknowledgements

The authors would like to thank N. Lochet and A. Jankowiak (LTMEx, CEA Saclay, France) for SPS sintering of the B_4C powders, C. Bachelet (IJCLab, Orsay, France) for the Li implantation at the IRMA implanter of the SCALP platform, J. Amalric (Science et Surface, Lyon, France) for TOF-SIMS measurements, and P. Sainsot (LaMCoS, INSA Lyon, France) for interferometry measurements.

Reference

[1]. V. Domnich, S. Reynaud, R. A. Haber, M. Chhowalla, J. Am. Ceram. Soc., 94- 11, 3605-3628 (2011), doi: 10.1111/j.1551-2916.2011.04865.x

[2]. M. Bouchacourt, F. Thevenot, J. Less Com. Met., 82, 227-235 (1981), doi: 10.1016/0022-5088(81)90223-X

[3]. D. Gosset, P. Herter, Matériaux absorbants neutroniques pour le pilotage des réacteurs. "Techniques de l'ingénieur", BN3720 (2007)

[4]. H. K. Clark, J. L. Koard, J. Am. Chem. Soc., 65, 2115-2119 (1943)

[5]. F. Thévenot, J. Eur. Ceram. Soc., vol. 6, no 4, p. 205-225, janv. 1990, doi: 10.1016/0955-2219(90)90048-K.

[6]. D. Gosset, Absorber materials for Generation IV reactors, in Structural Materials for Generation IV Nuclear Reactors, Elsevier, 533-567 (2017), https://linkinghub.elsevier.com/retrieve/pii/B978008100906200015X

[7]. D. Gosset, B. Provot, Prog. Nucl. Energy, 38-3-4, 263-266 (2001), doi: 10.1016/S0149-1970(00)00113-X.

[8]. D. Gosset, P. Herter, V. Motte, Nucl. Instrum. Methods Phys. Res. Sect. B Beam Interact. Mater. At., 434, 66-72 (2018), doi: 10.1016/j.nimb.2018.08.021.

[9]. A. Jostsons, C. K. H. DuBose, G. Copeland, J. O. Stiegler, J. Nucl. Mater., 49-2, 136-150 (1973), doi: 10.1016/0022-3115(73)90003-2.

[10]. G. W. Hollenberg, B. Mastel, J. A. Basmajian, J. Am. Ceram. Soc., 63-7-8, 376-380 (1980), doi: 10.1111/j.1151-2916. 1980.tb10195. x.

[11]. T. Stoto, N. Housseau, L. Zuppiroli, B. Kryger, J. Appl. Phys., 68-7, 3198-3206 (1990), doi: 10.1063/1.346370.

[12]. T. Maruyama, S. Onose, T. Kaito, H. Horiuchi, J. Nucl. Sci. Technol., 34-10, 1006-1014 (1997), doi: 10.1080/18811248.1997.9733777.

[13]. V. Motte, D. Gosset, G. Gutierrez, S. Doriot, N. Moncoffre, J. Nucl. Mater., 514, 334-347 (2019), doi: 10.1016/j.jnucmat.2018.12.012.

[14]. P. D. Kervalishvili, S. S. Shavelashvili, Sov. At. Energy, 57-1, 489-491 (1984), doi: 10.1007/BF01135831.

[15]. X. Deschanels, D. Simeone, J. P. Bonal, J. Nucl. Mater.,265-3, 321-324 (1999), doi: 10.1016/S0022-3115(98)00887-3.

[16]. J.E. Brocklehurst, B.T. Kelly, K.E Gilchrist, D. Mottershead, D.E.Y. Walker, S.D. Preston, Nucl. Energy 23-3, 179-189 (1984)

[17]. M.M. Oakden, B. Munro, J.E. Brocklehurst, B.T. Kelly, UK studies of the performance of boron carbide control rod pins for the fast reactor, Int. Conf. on Fast Reactor Core and Fuel Structural Behavior, part 5, Inverness (1990)

[18]. A. Schneider, G. Roma, J.P. Crocombette, V. Motte, D. Gosset, J. Nucl. Mater. 496, 157-162 (2017).

doi: 10.1016/j.jnucmat.2017.09.020.

[19]. Y. You, K. Yoshida, T. Yano, Jpn. J. Appl. Phys., 55-6, 640-648 (2018), doi: 10.7567/JJAP.57.055801

[20]. R. Matschat, A. Dette, S. Richter, S. Recknagel, P. Barth, J. Am. Ceram. Soc.,94-11, 4009–4016 (2011)

[21]. C.O. Bacri, C. Bachelet, C. Baumier, J. Bourçois, L. Delbecq, D. Ledu, N. Pauwels, S. Picard, S. Renouf, C. Tanguy., Nucl. Instrum. Methods Phys. Res. Sect. B.,406, 48-52 (2017), doi: 10.1016/j.nimb.2017.03.036.

[22]. J. F. Ziegler, U. Littmark, J. P. Biersack, Stopping and Ranges of Ions in Matter, Pergamon Press, New York (1985).

[23]. L. Zuppiroli, R. Kormann, D. Lesueur, Etude fondamentale du carbure de bore industriel, CEA-R-5237, https://inis.iaea.org/collection/NCLCollectionStore/_Public/15/005/15005581.pdf

[24]. R. G. Wilson, Int. J. Mass Spectr. Ion Process., 143, 43-49 (1995), doi: 10.1016/0168-1176(94)04136-U

[25]. A.D. Le Claire, Br. J. Appl. Phys. 14, 351-356 (1963)

[26]. B.A Chetroiu, Stress corrosion cracking of Alloy 600 in primary water of PWR: study of chromium diffusion, Thesis, Mines Paris-Tech (2015), https://pastel.archives-ouvertes.fr/tel-01157822

[27]. Y. Mishin, Chr. Herzig, Mat. Sci. Eng. A260, 55-71 (1999).

[28]. M. K. Linnarsson, M. S. Janson, S. Karlsson, A. Schöner, N. Nordell, et B. G. Svensson, Mater. Sci. Eng. B, 61-62, 275-280 (1999), doi: 10.1016/S0921-5107(98)00517-0

[29]. K. Persson, V.A. Sethuraman, L.J. Hardwick, Y. Hinuma, Y.S. Meng, A. van der Ven, V. Srinivasan, R. Kostecki, G. Ceder, J. Phys. Chem. Lett., 1, 8, 1176–1180 (2010)

[30]. L. Desgranges, J.M. Escleine, Ph. Bienvenu, I. Roure, D. Gosset, R. Böffi, U. Köster, Nucl. Inst. Meth. Phys. Res. B 432 42-47 (2018)

[31]. V. Motte, D. Gosset, T. Sauvage, H. Lecoq, N. Moncoffre, J. Nucl. Mater., 517, 165-174 (2019), doi: 10.1016/j.jnucmat.2019.02.012

[32]. A. Strasser, W. Yario, Control rod materials and burnable poisons: an evaluation of the state of the art and needs for technology development, July 1980. Final report, EPRI report NP 1974 (1981)